Structural and EPR studies of pyrophosphate-bridged dinuclear Cu[II] complexes

Rosana P. Sartoris [a,*], Rafael Calvo [a], Ricardo C. Santana [b], Otaciro R. Nascimento [c], Mireille Perec [d], Ricardo F. Baggio [e]

[a] Facultad de Bioquímica y Ciencias Biológicas, Universidad Nacional del Litoral and Instituto de Física del Litoral (CONICET-UNL), Güemes 3450, 3000 Santa Fe, Argentina
[b] Instituto de Física, Universidade Federal de Goiás, Campus Samambaia, CP 131, 74001-970 Goiânia, Brazil
[c] Grupo de Biofísica Molecular Sergio Mascarenhas, Departamento de Física e Informática, Instituto de Física de São Carlos, Universidade de São Paulo, CP 369, 13560-970 São Carlos-SP, Brazil
[d] Facultad de Ciencias Exactas y Naturales, DQIAQF-INQUIMAE, Universidad de Buenos Aires, Ciudad Universitaria, 1428 Buenos Aires, Argentina
[e] Comisión Nacional de Energía Atómica, Av. Gral Paz 1499, 1650 San Martín, Buenos Aires, Argentina

ABSTRACT

Two new pyrophosphate-bridged copper[II] complexes, $[Cu(dpa)(H_2O_7P_2)]_2$ **1** and $[Cu_2(terpy)_2(HO_7P_2)]_2 \cdot (H_2O_4P) \cdot (H_3O_4P) \cdot (H_2O)]$ **2** (dpa = 2,2′-dipyridylamine and terpy = 2,2′:6′,2″-terpyridine) were isolated and their crystal structures determined by single-crystal X-ray diffraction. The compounds are triclinic and contain dinuclear copper[II] units bridged by pyrophosphate anions. The EPR spectra observed in three planes of single crystal samples as a function of field orientation at 293 K for compounds **1** and **2**, and also for two other pyrophosphate compounds already reported, $[Cu(bipy)(cis-H_2O_7P_2)]_2 \cdot 3(H_2O)$ **3** and $[Cu(bipy)(trans-H_2P_2O_7)]_2$ **4** display a single resonance for any field orientation and temperatures T between 4 and 293 K, as in mononuclear spin systems, without hyperfine structure, and their g-factors and line widths were measured. The relations between the principal directions of the g-matrices and the molecular structures are discussed and compared with related compounds. The temperature dependences of the intensity of the EPR signals observed for **1**–**4** above 4 K indicate a paramagnetic Curie behavior, with no indication of intradinuclear exchange interactions (so, $|J| < 2$ K). The absence of dinuclear splitting and of hyperfine structure of the dinuclear units is explained in terms of averaging out by the interdinuclear interactions, allowing to set a lower limit of their magnitudes.

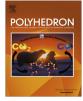© 2014 Elsevier Ltd. All rights reserved.

1. Introduction

The diphosphate tetra-anion $P_2O_7^{4-}$ (PPi), plays a central role in biochemical processes such as fat metabolism, and synthesis of proteins, DNA and RNA [1,2]. Bose et al. [3] and Ikotun et al. [4] demonstrated that monomeric Pt[II]/Pt[IV] and dinuclear Co[II]/Ni[II]/Cu[II] pyrophosphate compounds are toxic for drug-resistant cancer cell lines [5] and much research activity has been focalized on the coordination chemistry of PPi. As yet, the number of compounds containing metallic centers connected by pyrophosphate anions is still limited because of the known lability of the tetra-anion to hydrolysis, particularly in the presence of divalent metal ions, and to the associated difficulties for obtaining single crystals for X-ray studies [2,6–16]. To date, structural studies on these

materials have been mostly performed on samples obtained from solid state high-temperature syntheses and crystallizations. Alternatively a number of Cu[II] pyrophosphate-bridged compounds have been obtained using ancillary chelating ligands as heterocyclic imines and controlling the self-assembly of the Cu[II] species in presence of pyrosphosphate anions under different pH conditions. Thus, a variety of new compounds, dinuclear, polynuclear and 3D polymers were obtained and their structural, biological, electronic and magnetic properties investigated [2–18]. Nevertheless, magneto-structural studies of pyrophosphate-bridged Cu[II] metal complexes are yet scarce, and little is known about the capacity of the pyrophosphate bridges to support exchange interactions. The EPR technique provides information about the electronic structure and wave functions of the lowest energy states of the unpaired electrons and allow studying consequences of the Cu[II] dinuclear coordination of these structures. We report here the structures of the new compounds $[Cu(dpa)(H_2O_7P_2)]_2$ (dpa = 2,2′-dipyridylamine) **1** and (terpy = 2,2′:6′,2″-terpyridine) **2**. We also studied

the EPR spectra of single crystal samples of the compounds at ~9.9 and ~33.8 GHz. of the previously reported compounds and of [Cu(bipy)(cis-$H_2O_7P_2$)]$_2$·3(H_2O) **3** and [Cu(bipy)(trans-$H_2P_2O_7$)]$_2$ **4**, which were previously known and obtained as described in the literature [17,18]. We correlate the structure and the spectra of the four compounds in order to get a better understanding of the behavior of the pyrophosphate bridges.

2. Experimental section

2.1. Materials

All reagents, of commercially available reagent grade, were used without further purification. Aqueous solutions were prepared using reagent-grade deionized water (resistivity $\geqslant$ 18 MΩ/cm).

2.2. Preparations

2.2.1. Preparation of [Cu(dpa)($H_2O_7P_2$)]$_2$ **1**

Copper nitrate hemipentahydrate (0.24 g, 1 mmol), 2,2′-dipyridylamine (0.18 g, 1 mmol) and potassium pyrophosphate (0.70, 2 mmol) were added to 40 ml of water under stirring at 40 °C for two hours. Nitric acid was added to keep the pH around 2.5. The resulting suspension was filtered and the filtrate left standing at 40 °C, and after ~20 days dark green crystals of **1** suitable for the physical measurements separated out.

2.2.2. Preparation of [Cu$_2$(terpy)$_2$(HO$_7$P$_2$)·(H_2O_4P)·(H_3O_4P)·(H_2O)] **2**

Copper pyrophosphate (0.25 g, 1 mmol) and 2,2′:6′,2″-terpyridine (0.25 g, 1 mmol) were added to an alcohol–water (100 ml, 1:15) solution and the resulting suspension stirred for one week at room T. Perchloric acid was added to keep the pH at around 1.5. The suspension was filtered and the filtrate left standing for a month, and light green crystals of **2** suitable for X-ray diffraction and EPR measurements were isolated as the unique product.

2.3. Physical measurements

2.3.1. X-ray crystallography

Intensity measurements were obtained by means of an Oxford Diffraction Gemini CCD S Ultra diffractometer. For data collection, data reduction, and empirical absorption correction CRYSALIS-PRO [19] was used. Calculations to solve the structures, refine the models, and obtain derived results were carried out with the computer programs SHELXS-97 and SHELXL-97 [20], and for structure graphics SHELXTL [20], and MERCURY [21].

2.3.2. EPR techniques

EPR measurements were performed on single-crystal samples at room temperature using Bruker EMX plus (9.9 GHz) and Varian E110 (34.8 GHz) spectrometers, and between 4 and 293 K in a Bruker Elexsys E580 (9.4 GHz), with cavities, operating with 100 kHz field modulation. Calibration of the magnetic field $B_0 = \mu_0 H$ (μ_0 is the permeability of the vacuum) at the samples position and of line intensities, was achieved using dpph (g = 2.0035) and MgO:Cr^{III} (g = 1.9797) introduced in the sample holder as convenient field and signal intensity markers.

Since the triclinic structures of the four compounds introduce special difficulties in collecting and interpreting single crystal measurements, special techniques were required. Crystal habits were identified by measuring the angles between edges on each sample face with a goniometric optical microscope, and comparing the results with crystallographic information. Cubic sample holders made by cleaving pieces of KCl single crystals were used to define laboratory orthogonal reference frames **xyz** for the samples. The largest natural growth faces of the samples were glued on the xy faces of the holders, with an edge parallel to the holder edge, allowing obtaining the relationship between laboratory and crystal axes. The sample holders were mounted on top of a pedestal inside the cavity with one face (xy, yz or xz) parallel to the horizontal plane, and the orientation of B_0 was varied rotating the magnet. EPR spectra were collected in these orthogonal planes at 5° or 10° intervals. Positions of the axes **x**, **y** and **z** in these planes were determined within ~1° by comparing results in the three planes.

Table 1
Crystal data for compounds **1** and **2**.

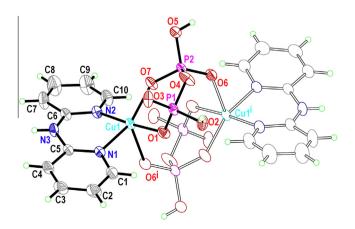| Code	1	2
Formula (Empirical)	[Cu(C$_{10}$H$_9$N$_3$)(H$_2$O$_7$P$_2$)]$_2$	Cu$_2$(C$_{15}$H$_{11}$N$_3$)$_2$(HO$_7$P$_2$) .(H$_2$O$_4$ P). (H$_3$O$_4$ P).(H$_2$ O)
Formula (Total)	C$_{20}$H$_{22}$Cu$_2$N$_6$O$_{14}$P$_4$	C$_{30}$H$_{30}$Cu$_2$N$_6$O$_{16}$P$_4$
Formula weight	821.40	981.56
Crystal system	triclinic	triclinic
Space group	$P\bar{1}$	$P\bar{1}$
a (Å)	8.023(2)	10.3843(5)
b (Å)	9.345(2)	14.3361(7)
c (Å)	10.868(2)	14.4160(8)
α	109.67(2)	60.569(5)
β	104.98(2)	88.835(4)
γ	103.19(2)	73.705(4)
V (Å^3)	695.3(3)	1776.26(19)
Z	1	2
Radiation, λ (Å)	Mo Kα, 0.71073	Mo Kα, 0.71073
μ (mm^{-1})	1.84	1.46
T (K)	294	294
ρ (g cm^{-3})	1.962	1.835
Crystal size (mm^3)	0.24 × 0.14 × 0.08	0.32 × 0.16 × 0.16
Transmission factors	0.76, 0.84	0.75, 0.79
Measured reflections	8749	86236
Independent reflections	3237	6951
Reflections with $I > 2\sigma(I)$	3098	5948
Parameters	220	555
Restraints	3	11
R_{int}	0.032	0.058
$R[F^2 > 2\sigma(F^2)]$	0.032	0.041
wR (F^2)	0.084	0.123
S	1.04	1.06
$D\rho_{max}$, $D\rho_{min}$ (e Å^{-3})	0.96, −0.52	0.59, −1.18

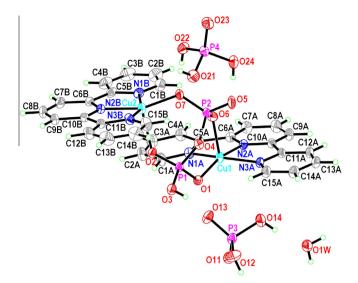**Fig. 1.** Molecular scheme of compound **1**, with displacement ellipsoids drawn at the 40% probability level.

Fig. 2. Molecular scheme of compound **2** with displacement ellipsoids drawn at the 40% probability level.

Fig. 3. Supramolecular structure of compound **1**, projected down **b**, showing the H-bonding interactions.

Table 2
Coordination lengths (Å) for **1** and **2**.

1			
Cu1–O1	1.9626 (18)	Cu1–N1	2.0056 (19)
Cu1–O7	1.9719 (17)	Cu1–O6^i	2.2601 (17)
Cu1–N2	1.980 (2)	Cu1–Cu1^i	4.5482 (14)
2			
Cu1–O1	1.918 (2)	Cu2–N2B	1.923 (3)
Cu1–N2A	1.932 (3)	Cu2–O7	1.923 (2)
Cu1–N1A	2.046 (3)	Cu2–N1B	2.054 (3)
Cu1–N3A	2.054 (3)	Cu2–N3B	2.064 (3)
Cu1–O6	2.190 (3)	Cu2–O2	2.190 (2)
		Cu1–Cu2	4.8982 (8)

Symmetry code (i) −x + 1, −y + 1, −z + 2.

3. Results and discussion

3.1. Crystallographic results

Crystal data for compounds **1** and **2** are summarized in Table 1; Figs. 1 and 2 display their molecular units defining the atom labeling schemes. Table 2 provides selected distances and angles and Table 3 details the H-bonding interactions. The dimeric unit in **1** (Fig. 1) is built up around an inversion centre, with one independent (dpa)Cu^{II} subunit and its inversion image linked by two symmetry related H$_2$PPh^{2-} anions. The structure of compound **2** (Fig. 2) consists of a fully independent dinuclear Cu$_2$terpy$_2$PPh group, with a central PPh^{4-} unit chelating two Cu^{II} centres at both sides, and two external terpy completing the cation coordination via their triple N,N',N'' bite. Structures of the previously described compounds **3** and **4** [17,18], display non-H cores quite similar to each other and to structure **1**, being built up around a symmetry centre. In compound **2** the PPh units bridge the Cu^{II} cations bi-chelating them in a μ$_2$κ^4 mode. Instead, in the structures of compounds **1**, **3** and **4**, each H$_2$PPh chelates one of the Cu^{II}, while linked in a monocoordinated way to its inversion image in a μ$_2$κ^3 fashion. In the four structures each copper cation is in a fivefold coordination environment: CuN$_3$O$_2$ type in **2**, (with N's from one terpy and O's from one single PPh tetraanion), and CuN$_2$O$_3$ type with N's from dpa or bipy and O's being provided only by symmetry related H$_2$PPh bianionic groups in **1**, **3** and **4**. The environments of the Cu atoms in fivefold coordination are conveniently described applying the τ descriptor [22], where τ = 0.00 characterizes a SP (square pyramid) and 1.00 a TB (trigonal bipyramid). Thus, the environments of Cu2 in **2** and Cu1 in **3** are rather perfect SP, with τ values of 0.01 and 0.00; while those around Cu1 in **2** and **4** deviate a little, but still leaning towards this type of description (τ values of 0.09 and 0.04, respectively). The Cu1 environment in **1** is between SP and TB geometries, with a τ value of

Table 3
Hydrogen-bond geometry for **1** and **2**.

N	**D**onor-**H**ydrogen···**A**cceptor	**D–H** (Å)	H···**A** (Å)	**D**···**A** (Å)	**D–H···A** (°)
Compound 1					
1	O5–H5O···O6^{ii}	0.82 (1)	1.85 (1)	2.652 (2)	170 (4)
2	O2–H2O···O3^{iii}	0.81 (1)	1.77 (1)	2.571 (3)	172 (4)
3	N3–H3N···O3^i	0.82 (1)	2.04 (1)	2.863 (3)	176 (3)
Symmetry codes: (i) −x + 1, −y + 1, −z + 1; (ii) −x, −y + 1, −z + 2; (iii) −x, −y, −z + 1.					
Compound 2					
1	O1W–H1WA···O23^i	0.84 (4)	2.01 (4)	2.837 (5)	166 (6)
2	O1W–H1WB···O23^{ii}	0.84 (5)	1.92 (5)	2.734 (6)	164 (4)
3	O3–H3···O13	0.84 (4)	1.69 (4)	2.513 (4)	168 (5)
4	O12–H12···O11^{iii}	0.86 (2)	1.65 (2)	2.507 (4)	175 (4)
5	O14–H14···O1W	0.84 (6)	1.81 (6)	2.644 (6)	173 (6)
6	O21–H21···O13^{iv}	0.86 (4)	1.73 (4)	2.540 (5)	158 (5)
7	O22–H22···O7	0.85 (8)	1.77 (8)	2.618 (4)	174 (7)
8	O24–H24···O5	0.85 (7)	1.64 (7)	2.474 (6)	169 (6)
Symmetry codes: (i) −x + 2, −y + 1, −z; (ii) x, y + 1, z; (iii) −x + 1, −y + 2, −z; (iv) −x + 1, −y + 1, −z.					

0.36. Structures **1** and **4** are unsolvated, while structures **2** and **3** are completed by a diversity of solvates and/or counterions, in a rather complex way. Structure **1** displays a simple 3D supramolecular structure, linked by three different H-bonds, almost perpendicular to each other, described in Table 3 and shown in Fig. 3, where they have been identified by their order number in the table. All three take part in three centrosymmetric loops. The first two involve phosphate donors and are labelled in Fig. 3 as ring A $\{R(8)_2^2$, $(a + a^{ii})$, $a = [P2–O5–H5O\cdots O6^{ii}]$; (ii) $-x$, $-y + 1$, $-z + 2\}$ and ring B $\{R(8)_2^2$, $(b + b^{iii})$, $b = [P1–O2–H2O\cdots O3^{iii}]$, (iii) $-x$, $-y$, $-z + 1\}$. The third one, involves the amino H and gives rise to a larger loop, C $\{R(16)_2^2$, $(c + c^i)$, $c = [P1–O1–Cu1–N2–C6–N3–H3N\cdots O3^i]$, (i) $-x + 1$, $-y + 1$, $-z + 1\}$. Finally, there is a larger, non-symmetric $R(14)_3^2$ loop (D in Fig. 3) embedded among the preceding three loops and sharing one H-bond with each one of them. In the case of structure **2** the dimer bears a single positive charge due to the existence of an H atom at O3 (and its symmetry related O3'); charge balance is then achieved through a $[PO_4H_2]^-$ counter anion, and the structure completed by neutral $[PO_4H_3]$ and H_2O molecules. The large availability of H

bonding donors and acceptors promotes the formation of an intricate H-bonding net parallel to (0 0 1). Fig. 4a shows a scheme where only the intervening groups are represented (Cu and terpy not shown) and where H-bonds have been identified by their order number in Table 3. The main features are six independent H-bonded loops of different size and degree, tightly concatenated to define the 2D structure. Four of them build up around symmetry centres. Two of them are rather small and amenable of a thorough description, viz., loop A $\{R(8)_4^2$, $a + a^x$; $a = [\cdots H1WB–O1W–H1WA\cdots O23^i]$; (i) $-x + 2$, $-y + 1$, $-z$; ($\boldsymbol{x}$) $-x + 2$, $-y + 2$, $-z\}$, loop B $\{R(8)_2^2$, $b + b^{iii}$; $b = [P3–O12–H12\cdots O11^{iii}]$; (iii) $-x + 1$, $-y + 2$, $-z\}$. The remaining two centrosymmetric loops are much larger, viz.: D: $\{R(32)_8^8$, involving entries 1, 3, 5 and 7 in Table 3$\}$ and E $\{R(24)_6^4$, involving entries 3, 6 and 7/8$\}$ and are better described by inspection of Fig. 4a.

The two non-centrosymmetric rings which complete the most relevant closed structures appear "sandwiched" between the latter centrosymmetric ones; they are loops C $\{R(14)_4^4$, surveying entries 2, 4, 5 and 6 in Table 3 (structure 2)$\}$ and F $\{R(8)_2^2$, involving entries 7 and 8$\}$ (for nomenclature, see Bernstein et al. [23]). The terpy
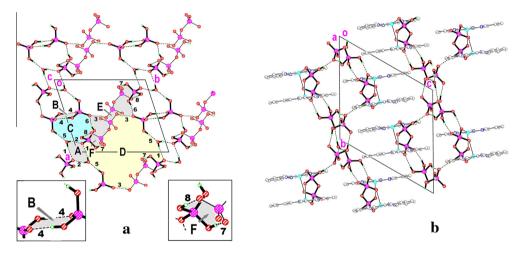

Fig. 4. Supramolecular structure of compound **2**. (a) Projection along **c**, showing the H-bonding network (Cu and terpy not shown, for clarity). Loops B and F, of difficult appreciation in the figure are clarified in the insets. (b) Projection along **a**, showing the way in which interdigitation takes place.
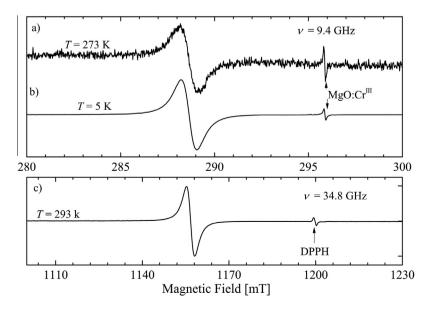

Fig. 5. EPR spectrum of compound **3** at X and Q bands, and different temperatures. The small peak corresponds to the used marker. A similar single peak is observed at any field orientation at room T for the four compounds, and that was also verified for a single orientation of B_0 between 4 and 293 K.

groups, not shown in Fig. 4a, protrude outwards the planes, and interact with their counterparts in neighboring planes. This lateral interaction takes place in a 2:2 interdigitation way (Fig. 4b), as opposed to the 1:1 interdigitation observed in **1**.

3.2. EPR results and modeling

Since the crystal symmetry and the local symmetries at the copper ions are low, EPR in powder samples of **1** and **2** are of little use, and the measurements presented here were performed in oriented single crystals which provide much more information. EPR spectra of crystals of **1–4** were collected in the orthogonal planes *xy*, *xz* and *yz* described in the experimental section at 293 K, at 9.9 and 34.8 GHz. Results at 9.9 GHz do not add new information, and are not shown.

Fig. 5 displays the spectra of compound **3** at 9.4 GHz and 273 and 5 K, and at 34.8 GHz and 293 K. All of them show a single
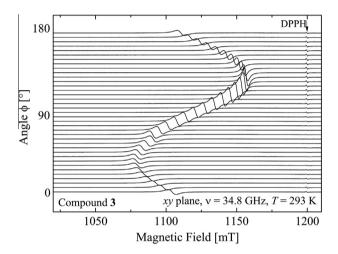
resonance without dinuclear or hyperfine splittings for any field orientation at any temperature. The same result is shown by the other three compounds. Fig. 6 displays the variation with the orientation of B_0 of this single resonance for the case of compound **3** in the *xy* laboratory plane. Similar results obtained in the three studied planes of compounds **1–4**, allowed to calculate the g^2-factors and widths of the resonances as a function of the orientation of B_0 by least squares fits of Lorentzian derivative line shapes to the observed spectra. The g^2-factor as a function of field orientation in the three planes is displayed in Fig. 7a–d for the four compounds, and these data allowed to calculate the g^2-matrices in the laboratory frame (see below).

In addition, the EPR spectra of crystals of **1–4** with B_0 oriented in the **xy** plane in the directions indicated with arrows in Fig. 5, were studied at 9.4 GHz as a function of *T* between 4 and 293 K. A single line was observed along this *T* range, and the areas of these lines were calculated to study their temperature dependences [24,26,27]. The results, displayed in Fig. 8a–d (normalized to the area observed at 293 K), show Curie (1/*T*) dependences (see solid lines) indicating that compounds **1–4** are paramagnetic above ∼4 K. To discard contributions due to changes of the experimental setup with *T* affecting the validity of these results, the area of the signal of the marker was also calculated together with each compound (MgO:Cr[III] is paramagnetic in the studied paramagnetic range), observing the same Curie behavior. The results in Fig. 8a–d indicate that the intradinuclear exchange interaction $|J_0| < 2$ cm^{-1} for compounds **1–4**.

When spins S_{Cu_1} and S_{Cu_2} in dinuclear molecules are exchange coupled, singlet and triplet states are split by the intradinuclear exchange coupling J_0, and the EPR spectra are described by the spin Hamiltonian [25–27]:

$$\mathcal{H}_1 = \mu_B \, \boldsymbol{B_0} \cdot (\boldsymbol{g_{Cu_1}} \cdot \boldsymbol{S_{Cu_1}} + \boldsymbol{g_{Cu_2}} \cdot \boldsymbol{S_{Cu_2}}) - J_0 \, \boldsymbol{S_{Cu_1}} \cdot \boldsymbol{S_{Cu_2}} + \boldsymbol{S_{Cu1}} \cdot \boldsymbol{D} \cdot \boldsymbol{S_{Cu_2}} + \mathcal{H}' \quad (1)$$

where $\boldsymbol{g_{Cu_1}}$ and $\boldsymbol{g_{Cu_2}}$ are the g-matrices, J_0 is the intradinuclear exchange interaction and the traceless spin–spin interaction matrix $\boldsymbol{D}$ considers dipole–dipole and anisotropic exchange, which split the EPR spectra of the triplet state [27]. $\mathcal{H}'$ considers weaker isotropic exchange couplings between neighbor dinuclear molecules. The EPR spectrum predicted by eq. 1 behaves as that of an effective spin

Fig. 6. Angular variation of $g^2(\theta,\phi)$ at *T* = 293 K and 33.8 GHz for compound **3** with B_0 applied in the **xy** plane of the laboratory system defined in the text. Similar measurements were performed in the three planes *xy*, *xz* and *yz*, for the four compounds.
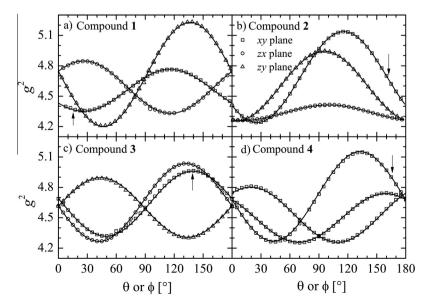

Fig. 7. Angular variation of the squared g-factor for compounds **1–4**, at 33.8 and 293 K. The solid lines are calculated with the components of the g^2 matrices a 33.8 GHz, given in Table 4.
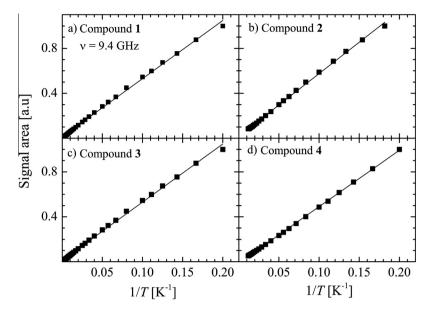
Fig. 8. Temperature variations of the area of the single peak of the spectra corresponding to compounds **1–4**, between 4 and 293 K. In all cases the results were normalized so the area at 293 K was taken as unity. The solid lines are obtained from fits of $1/T$ dependences to the data. The magnetic field orientations where these results were obtained are indicated by arrows in Fig. 7.

triplet $S = 1$, with two allowed transitions, $S_z = \pm1 \leftrightarrow 0$, and in certain cases a forbidden transition $S_z = \pm1 \leftrightarrow \mp1$ [25–27]. The splitting J_0 does not affect the shape or structure of the resonances but produces a T variation of their intensities proportional to the magnetic susceptibility. For antiferromagnetic units the signals disappear at $k_BT \ll |J_0|$, when the excited triplet state is unpopulated [24,27]. This does not occur in our measurements, setting the upper limit $|J_0| < 2$ K, according the studied range of T. The $\boldsymbol{D}$ term varies the splitting of the allowed resonances with the orientation of B_0. We do not observe hyperfine coupling and thus we do not include in Eq. (1) these terms between the electronic and nuclear spins of copper.

Instead of the behavior predicted by Eq. (1), the EPR results between 4 and 293 K in Figs. 5 and 8 indicate no exchange coupling ($|J_0| < 2$ cm^{-1}) and no structure arising from anisotropic spin–spin interactions ($|D| < 3 \times 10^{-4}$ cm^{-1}) which could be assigned to the dinuclear structure. So,

$$\mathcal{H}_1 = \mu_B \, \boldsymbol{S} \cdot \boldsymbol{g} \cdot \boldsymbol{B}_0 \qquad (2)$$

and the position of the single resonance observed for each $\boldsymbol{B_0} = B_0$ ($\sin\theta\cos\phi$, $\sin\theta\sin\phi$, $\cos\theta$) allows obtaining $g^2(\theta,\phi)$ and the components of the $\boldsymbol{g^2}$-matrix using [28,29]:

$$
\begin{aligned}
g^2(\theta,\phi) &= (g^2)_{xx}\sin^2\theta\cos^2\phi + (g^2)_{yy}\sin^2\theta\sin^2\phi + (g^2)_{zz}\cos^2\theta \\
&\quad + 2(g^2)_{xy}\sin^2\theta\sin\phi\cos\phi + 2(g^2)_{xz}\sin\theta\cos\theta\cos\phi \\
&\quad + 2(g^2)_{yz}\sin\theta\cos\theta\sin\phi
\end{aligned}
$$

The results, given in Table 4, include the eigenvalues and eigenvectors of $\boldsymbol{g^2}$ calculated from the data in Fig. 7a–d. The lines in these figures, obtained with these values, are in excellent agreement with data. The inversion symmetry centers relating Cu^{II} ions in compounds **1**, **3** and **4**, require $\boldsymbol{g}_{Cu_1} = \boldsymbol{g}_{Cu_2}$, as it is observed. This symmetry does not occur in compound **2** where $\boldsymbol{g}_{Cu_1}$ and $\boldsymbol{g}_{Cu_2}$ should be different, producing in principle different resonances. Thus, the experimental result of a single peak indicates that the resonances of the two coppers in **2** collapse due to the exchange interactions and $\boldsymbol{g}_{Cu_1}$ and $\boldsymbol{g}_{Cu_2}$ are replaced by their average $<\boldsymbol{g}> = (\boldsymbol{g}_{Cu_1} + \boldsymbol{g}_{Cu_2})/2$ [30–33].

Table 4
(a) Components of the $\boldsymbol{g^2}$ matrices calculated from the single crystal EPR data at room temperature and 33.8 GHz for **1–4** in the $\boldsymbol{xyz}$ orthogonal laboratory frame of axes at 293 K. (b) and (c) contain the eigenvalues and eigenvectors of these matrices.

	1	**2**	**3**	**4**
(a)				
$(g^2)_{xx}$	4.431(1)	4.409(1)	4.688(1)	4.741(1)
$(g^2)_{yy}$	4.684 (1)	4.952(1)	4.590(1)	4.319(1)
$(g^2)_{zz}$	4.745 (1)	4.264(1)	4.614(1)	4.677(1)
$(g^2)_{xy}$	−0.162(1)	−0.351(1)	−0.318(1)	0.172(1)
$(g^2)_{xz}$	0.205(1)	−0.026(1)	−0.383(1)	−0.441(1)
$(g^2)_{yz}$	−0.512 (1)	−0.064(1)	0.294(1)	−0.161(1)
(b)				
$(g^2)_1$	4.199 (6)	4.195(1)	4.266(1)	4.257(1)
$(g^2)_2$	4.357 (1)	4.303(1)	4.325(1)	4.267(1)
$(g^2)_3$	5.306 (1)	5.127(1)	5.300(1)	5.213(1)
(c)				
$\boldsymbol{a}_1$	−0.134(9)	−0.692(1)	0.42(1)	0.14(9)
	0.697(2)	−0.373(1)	0.852(7)	−0.96(1)
	0.704(1)	−0.617(1)	−0.30(1)	−0.2(1)
$\boldsymbol{a}_2$	0.948(1)	0.574(1)	0.648(1)	0.69(3)
	0.295(7)	0.232(1)	−0.05(1)	−0.0(1)
	−0.111(6)	−0.784(1)	0.75(1)	0.72(3)
$\boldsymbol{a}_3$	0.286(1)	−0.437(1)	0.630(1)	−0.709(1)
	−0.653(1)	0.897(1)	−0.520(1)	−0.254(1)
	0.701 (1)	−0.053(1)	−0.570(1)	0.659(1)

4. Discussion and conclusions

The new compounds **1** and **2** show dinuclear crystal structures as the previously reported pyrophosphate compounds **3** and **4**; however, each one displays their own characteristic 3D structures which are described above. At 293 K we observe in compounds **1–4** single EPR peaks without the expected dinuclear spectral structure (allowing to say that $|D| < 3 \times 10^{-4}$ cm^{-1}) and hyperfine couplings with the nuclear spins of copper, for any magnetic field orientation. This single peaks were verified for a single field orientation in all four compounds, in the full range of T between 4 and 293 K. In compound **2** where Cu$_1$ and Cu$_2$ ions are not related by a symmetry operation and two resonances would be expected, we observe that these two resonances are fully merged by the exchange coupling,
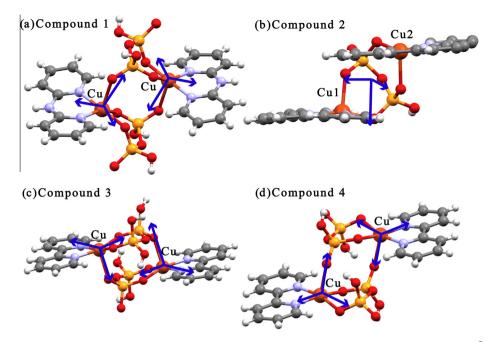
Fig. 9. Schemes displaying the structures of the copper dinuclear units of the compound **1**, **2**, **3** and **4** together with the principal axes of the $\boldsymbol{g^2}$-matrices obtained from the EPR data.

Table 5
(a) Growth faces glued to the sample holder (see Ref. [30]) and normal to this face, (b) Crystal direction chosen in this plane, (c) in terms of the set of orthogonal crystal axes, (d) Normal to the planes which best fit the equatorial ligands to the Cu^{II} ions calculated from the crystallographic data, (e) Eigenvectors corresponding to the axial direction g_3 of the g^2 matrices for compounds **1** to **4**, (f) Angles between the directions given in (d) and (e).

	1	**2**	**3**	**4**
(a) Face	*bc* ($\boldsymbol{a^*}$)	*ab* ($\boldsymbol{c^*}$)	*ac* ($\boldsymbol{b^*}$)	*ab* ($\boldsymbol{c^*}$)
(b) Edge	$\boldsymbol{y \equiv -c}$	$\boldsymbol{y \equiv b}$	$\boldsymbol{y \equiv c}$	$\boldsymbol{x \equiv a}$
(c) Laboratory axes	$\boldsymbol{a^*b^*c}$	$\boldsymbol{a^*bc^*}$	$\boldsymbol{a^*b^*c}$	$\boldsymbol{a^*b^*c}$
(d) Crystallographic normal	−0.159	<n>=−0.381	0.671	0.706
	0.691	0.915	−0.463	0.285
	−0.704	−0.134	−0.579	−0.648
(e) $(g^2)_3$ direction	−0.286(1)	−0.437(1)	0.6308(1)	0.709(1)
	0.653(1)	0.897(1)	−0.521(1)	0.254(1)
	−0.701(1)	−0.053(1)	−0.575(1)	−0.659(1)
(f) Angle (°)	8.6°	5.7°	4.0°	1.9°

and the calculated $\boldsymbol{g^2}$-matrix is the average of the molecular $\boldsymbol{g^2}$-matrices of the individual Cu ions. We plot in Fig. 9a–d the dinuclear molecular cores of **1**–**4** together with the directions of the eigenvectors corresponding to the eigenvalues $(g^2)_1$, $(g^2)_2$, and $(g^2)_3$ of the $\boldsymbol{g^2}$ matrices, which are given in Table 4. To do that, we used the relations between the laboratory axes $\boldsymbol{xyz}$ of the EPR measurements described before, and the crystal axes $\boldsymbol{abc}$ and the orthogonal bases $\boldsymbol{ab^*c^*}$, $\boldsymbol{a^*bc^*}$ or $\boldsymbol{a^*b^*c}$ [34] listed in Table 5. Using the crystallographic data and the MERCURY program [21], we calculated the normal $\boldsymbol{n}$ to the planes of ligands of the Cu^{II} ions in compounds **1, 3**, and **4**, and the average $<\boldsymbol{n}> = (\boldsymbol{n_1} + \boldsymbol{n_2})/2$ in compound **2**, in the axes $\boldsymbol{xyz}$ and the angles between the normals and the axial directions corresponding to the eigenvalue $(g^2)_3$, see Table 5. Thus, Fig. 9a–d shows the correlations between EPR and structural results, particularly the normal to the $d(x^2 - y^2)$ ground orbital of the Cu^{II} ions.

The modulus of the expected intradinuclear anisotropic spin–spin interaction D can be estimated summing the two contributions [35,36], dipole–dipole interaction $|D_{\mathrm{dip}}| \sim \frac{3}{2} \frac{g^2 \mu_B^2}{R_{\mathrm{Cu-Cu}}^3}$ and anisotropic exchange $|D_{\mathrm{anis}}| \sim \left(\frac{\Delta g}{g}\right)^2 J_0$, where $R_{\mathrm{Cu-Cu}}$ is the distance between copper ions in a dinuclear unit, J_0 is the exchange coupling and g and Δg are the average and the anisotropy of the g-factor. So, $|D_{\mathrm{dip}}|$ is

between 0.072 and 0.044 cm^{-1} and $|D_{\mathrm{anis}}| < 0.03$ cm^{-1}. To average out the dinuclear structures, as it is observed, the exchange interactions between neighbor dinuclear units should be larger than these couplings [37], or $|J'| \geqslant 0.07$ cm^{-1}. These interactions are supported by weak couplings as H-bonds and π–π stacking interactions. These magnitudes are also sufficient to average out the hyperfine couplings of Cu^{II} ions with their nuclei. EPR line widths similar at 9.9 and 34.8 GHz show a complicate angular variation due to the low symmetry of the crystal structures. They result from the dipolar interactions between coppers, narrowed by an intricate network of weak intra and interdinuclear exchange couplings.

Appendix A. Supplementary data

CCDC 973087 and 973088, contains the supplementary crystallographic data for **1** and **2**. These data can be obtained free of charge via http://www.ccdc.cam.ac.uk/conts/retrieving.html, or

from the Cambridge Crystallographic Data Centre, 12 Union Road, Cambridge CB2 1EZ, UK; fax: (+44) 1223 336 033; or e-mail: deposit@ccdc.cam.ac.uk.

References

[1] J.M. Berg, J.L. Tymoczko, L. Stryer, Biochemistry, fourth ed., W. H. Freeman and Company, New York, 2001.
[2] O.F. Ikotun, N. Marino, P.E. Kruger, M. Julve, R.P. Doyle, Coord. Chem. Rev. 254 (2010) 890.
[3] R.N. Bose, L. Maurmann, R.J. Mishur, L. Yasui, S. Gupta, W.S. Grayburn, H. Hofstetter, T. Salley, Proc. Natl. Acad. Sci. U.S.A. 105 (2008) 18314.
[4] O.F. Ikotun, E.M. Higbee, W. Ouellette, R.P. Doyle, J. Inorg. Biochem. 103 (2009) 1254.
[5] N. Marino, A.R. Vortherms, A.E. Hoffman, R.P. Doyle, Inorg. Chem. 49 (2010) 6790.
[6] P. Heikinheimo, P. Pohjanjoki, A. Helminen, M. Tasanen, B.S. Cooperman, A. Goldman, A. Baykov, R. Lahti, Eur. J. Biochem. 239 (1996) 138.
[7] J.-Y. Xu, J.-L. Tian, Q.-W. Zhang, J. Zhao, S.-P. Yan, D.-Z. Liao, Inorg. Chem. Commun. 11 (2008) 69.
[8] E.W. Ainscough, A.M. Brodie, J.D. Ranford, J.M. Waters, K.S. Murray, Inorg. Chim. Acta 197 (1992) 107.
[9] P.E. Kruger, R.P. Doyle, M. Julve, F. Lloret, M. Nieuwenhuyzen, Inorg. Chem. 40 (2001) 1726.
[10] R.P. Doyle, P.E. Kruger, B. Moubaraki, K.S. Murray, M. Nieuwenhuyzen, Dalton Trans. (2003) 4230.
[11] R.P. Doyle, M. Nieuwenhuyzen, P.E. Kruger, Dalton Trans. (2005) 3745.
[12] R.P. Doyle, T. Bauer, M. Julve, F. Lloret, J. Cano, M. Nieuwenhuyzen, P.E. Kruger, Dalton Trans. (2007) 5140.
[13] O.F. Ikotun, N.G. Armatus, M. Julve, P.E. Kruger, F. Lloret, M. Nieuwenhuyzen, R.P. Doyle, Inorg. Chem. 46 (2007) 6668.
[14] O.F. Ikotun, E.M. Higbee, W. Ouellette, F. Lloret, M. Julve, R.P. Doyle, Eur. J. Inorg. Chem. (2008) 5281.
[15] N. Marino, C.H. Fazen, J.D. Blakemore, C.D. Incarvito, N. Hazari, R.P. Doyle, Inorg. Chem. 50 (2011) 2507.
[16] N. Marino, S.K. Hanson, P. Müller, R.P. Doyle, Inorg. Chem. 51 (2012) 10077.
[17] N. Marino, O.F. Ikotun, M. Julve, F. Lloret, J. Cano, R.P. Doyle, Inorg. Chem. 50 (2011) 378.
[18] M. Perec, R.P. Sartoris, R. Calvo, R. Baggio, Chem. Commun. 22 (2012) 141.
[19] Oxford. Diffraction, CRYSALIS PRO, Oxford Diffraction Ltd, Abingdon, Oxfordshire, England, 2009.
[20] G.M. Sheldrick, Acta Crystallogr., Sect. A 64 (2008) 112.
[21] C.F. Macrae, I.J. Bruno, J.A. Chisholm, P.R. Edgington, P. McCabe, E. Pidcock, L. Rodriguez-Monge, R. Taylor, J. van de Streek, P.A. Wood, J. Appl. Crystallogr. 41 (2008) 466.
[22] A.W. Addison, T.N. Rao, J. Reedijk, J. Van Rijn, G.C. Verschoor, J. Chem. Soc., Dalton Trans. (1984) 1349.
[23] J. Bernstein, R.E. Davis, L. Shimoni, N.-L. Chang, Angew. Chem., Int. Ed. Engl. 34 (1995) 1555.
[24] J.R. Wasson, C.-I. Shyr, C. Trapp, Inorg. Chem. 7 (1968) 469.
[25] M. Perec, R. Baggio, R.P. Sartoris, R.C. Santana, O. Peña, R. Calvo, Inorg. Chem. 49 (2010) 695.
[26] B. Bleaney, K.D. Bowers, Proc. R. Soc. A London Math. Phys. Sci. 214 (1952) 451.
[27] J.A. Weil, J.R. Bolton, Electron Paramagnetic Resonance: Elementary Theory and Practical Applications, Wiley-Interscience, New York, 2007.
[28] R. Calvo, S.B. Oseroff, H.C. Abache, J. Chem. Phys. 72 (1980) 760.
[29] R.C. Santana, B.N. Ferreira, J.R. Sabino, J.F. Carvalho, O. Peña, R. Calvo, Polyhedron 47 (2012) 53.
[30] a R. Calvo, M.A. Mesa, Phys. Rev. B 28 (1983) 1244;
b R. Calvo, M.A. Mesa, G. Oliva, J. Zukerman-Schpector, O.R. Nascimento, M. Tovar, R.J. Arce, Chem. Phys. 81 (1984) 4584.
[31] A.M. Gennaro, P.R. Levstein, C.A. Steren, R. Calvo, Chem. Phys. 111 (1987) 431.
[32] P.R. Levstein, R. Calvo, E.E. Castellano, O.E. Piro, B.E. Rivero, Inorg. Chem. 29 (1990) 3918.
[33] R. Calvo, Appl. Magn. Reson. 31 (2007) 271.
[34] C. Giacovazzo, Fundamentals of Crystallography, third ed., Oxford Science Publications, Oxford, 2011.
[35] A. Bencini, D. Gatteschi, Electron Paramagnetic Resonance of Exchange Coupled Systems, Springer-Verlag, Berlin, 1990.
[36] T. Moriya, Phys. Rev. 120 (1960) 91.
[37] M.C.G. Passeggi, R. Calvo, J. Magn. Reson. A 114 (1995) 1.